




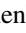





Spatially Resolved Broadband Synchrotron Emission from the Nonthermal Limbs of SN1006

Jiang-Tao Li¹ , Jean Ballet² , Marco Miceli^{3,4} , Ping Zhou⁵ , Jacco Vink⁵ , Yang Chen⁶ , Fabio Acero²,
Anne Decourchelle², and Joel N. Bregman¹ 

¹ Department of Astronomy, University of Michigan, 311 West Hall, 1085 S. University Avenue, Ann Arbor, MI, 48109-1107, USA

² Service d'Astrophysique, CEA Saclay, F-91191 Gif-sur-Yvette Cedex, France

³ Dipartimento di Fisica and Chimica, Università di Palermo, Piazza del Parlamento 1, I-90134 Palermo, Italy

⁴ INAF-Osservatorio Astronomico di Palermo, Piazza del Parlamento, I-90134 Palermo, Italy

⁵ Anton Pannekoek Institute/GRAPPA, University of Amsterdam, P.O. Box 94249, 1090 GE Amsterdam, The Netherlands

⁶ Department of Astronomy, Nanjing University, Nanjing 210023, People's Republic of China

Received 2018 May 25; revised 2018 July 12; accepted 2018 July 22; published 2018 August 31

Abstract

We present ~ 400 ks *NuSTAR* observations of the northeast (NE) and southwest (SW) nonthermal limbs of the Galactic SNR SN1006. We discovered three sources with X-ray emission detected at $\gtrsim 50$ keV. Two of them are identified as background active galactic nuclei. We extract the *NuSTAR* spectra from a few regions along the nonthermal limbs and jointly analyze them with the *XMM-Newton* spectra and the radio data. The broadband radio/X-ray spectra can be well described with a synchrotron emission model from a single population of CR electrons with a power-law energy distribution and an exponential cutoff. The power-law index of the electron particle distribution function (PDF) is ≈ 1.88 – 1.95 for both the NE and SW limbs, and we do not find significant evidence for a variation of this index at different energy (curvature). There are significant spatial variations of the synchrotron emission parameters. The highest energy electrons are accelerated in regions with the lowest expansion velocity, which is opposite to what has been found in Tycho's supernova remnant. In addition to a gradual steepening of synchrotron emission from the center of the nonthermal limbs to larger azimuthal angles, we also find that both the emission spectrum and the PDF are significantly flatter in three regions in the SW limb where the shock encounters a higher density ambient medium. The NE limb also shows significantly higher cutoff energy in the PDF than the SW limb. By comparing with the roughly symmetric TeV emission and largely asymmetric GeV emission from the two nonthermal limbs, we conclude that the asymmetry in the ambient medium and magnetic fields may have largely modified the acceleration and emission of CR leptons.

Key words: acceleration of particles – cosmic rays – ISM: supernova remnants – radiation mechanisms: non-thermal – shock waves – X-rays: ISM

Supporting material: figure set

1. Introduction

Supernova remnants (SNRs) are thought to be efficient sites accelerating cosmic rays (CRs) up to the “knee” of the Galactic CR spectrum (at $\sim 3 \times 10^3$ TeV; e.g., Blandford & Eichler 1987; Blasi 2013). Nonthermal emissions in radio and hard X-rays associated with young SNRs are often best modeled with synchrotron emission of leptonic CRs and thus have been adopted as direct evidence of shock acceleration of CR particles (e.g., Koyama et al. 1995). The shape of the particle distribution function (PDF) responsible for the synchrotron emission is often characterized by two key parameters: the slope and cutoff energy. The slope of the PDF can be modified by nonlinear acceleration processes and other microphysics (e.g., Caprioli 2012), while the cutoff energy, or typically the maximum energy a shock-accelerated particle can reach, could be limited by a few physical processes, such as the synchrotron radiative loss, the limited acceleration time, and the change of the available magnetohydrodynamic (MHD) waves above some wavelength (known as loss-, time-, or escape-limited accelerations; e.g., Reynolds 2008).

The remnant of the supernova (SN) AD1006 (SN1006) is of particular scientific interest as a well known site of CR acceleration in a relatively clean environment (high Galactic latitude with no significant molecular cloud, e.g., Dubner

et al. 2002). The nonthermal nature of the X-ray spectrum was suggested as early as in the *Einstein* era (e.g., Becker et al. 1980), and was confirmed with *ASCA* observations (Koyama et al. 1995). In the two prominent limbs located in the northeast (NE) and southwest (SW) quarter of the SNR shell, the radio/X-ray correspondence is striking even in fine structures, suggesting that the nonthermal hard X-ray emission is primarily synchrotron radiation produced by the same population of shock-accelerated electrons responsible for the radio emission (e.g., Winkler & Long 1997). Later, *Chandra* and *XMM-Newton* observations resolved the fine structures of the nonthermal filaments (e.g., Bamba et al. 2003; Long et al. 2003), and revealed significant spatial variations of the synchrotron emission parameters (e.g., Rothenflug et al. 2004; Allen et al. 2008; Miceli et al. 2009, 2014; Li et al. 2015).

Observing the spatial variation of the shape of multi-wavelength synchrotron spectrum provides us with a lot of information about the physics of particle acceleration, such as the energy spectrum of the accelerated electrons, the strength and structure of the magnetic field, and the physical mechanisms limiting the maximum energy achieved by the accelerated electrons, etc. (Reynolds 2008). Dyer et al. (2001) jointly fitted the available X-ray, radio, and TeV data and found that extrapolating from the measured radio fluxes grossly

overpredicts the X-ray flux. Bamba et al. (2008) make use of the wide-band *Suzaku* observations to determine the roll-off frequency of the power law in X-rays, and found it is significantly higher in the NE than in the SW. Katsuda et al. (2010) found that there is a spatial correlation between the nonthermal X-ray flux and the cutoff frequency in the NE limb. This result may indicate that the cutoff frequency depends on the magnetic-field strength, which is a natural prediction of the time- or escape-limited scenario, but not the loss-limited scenario (Reynolds 2008). However, Miceli et al. (2013) found that a synchrotron radiative loss-limited model provides a better fit to all the X-ray spectra of the nonthermal limbs than acceleration-time-limited or escape-limited models. These different conclusions can be reconciled in a loss-limited scenario if the rate of particle injection and/or acceleration depends on some effects not yet accounted for, e.g., the shock obliquity.

Previous modeling of the broadband synchrotron emission from radio to hard X-ray in SNRs is often limited by two issues: (1) The radio data either lacks spatial resolution in single-dish observations or is inaccurate in flux due to the limited u , v coverage in interferometry observations. (2) The soft X-ray emission at $\lesssim(1-2)$ keV is often dominated by the thermal component and the hard X-ray emission at $\gtrsim(7-8)$ keV has low resolution and sensitivity.

In this paper, we present spatially resolved joint analyses of the broadband synchrotron spectra from the two nonthermal limbs of SN1006, based on the high-resolution flux-accurate radio image from Dyer et al. (2009), the archival *XMM-Newton* data analyzed in Li et al. (2015, 2016), and a large *NuSTAR* program approved in Cycle 1. We will present an analysis of the *NuSTAR* data in Section 2, a joint analysis of the radio, *XMM-Newton*, and *NuSTAR* spectra in Section 3, and discuss the results in Section 4. The conclusions are summarized in Section 5. Errors are quoted at the 1σ confidence level throughout the paper.

2. *NuSTAR* Data Calibration and Analysis

2.1. *NuSTAR* Data Calibration

NuSTAR observations of the two nonthermal limbs of SN1006 are approved in Cycle 1 (2015-04-01—2016-04-30; PI: Jiang-Tao Li) and are taken on 2016-03-02 [northeast (NE) limb; OBSID=40110001001 and 40110001002] and 2016-03-08 [southwest (SW) limb; OBSID=40110002001 and 40110002002], respectively, each lasting ~ 200 ks (Figure 1).

We reprocess the *NuSTAR* data using the standard *NuSTAR* pipeline data reduction tool *nupipeline*. We have applied strict criteria regarding passages through the South Atlantic Anomaly (SAA) and a “tentacle”-like region of higher activity near part of the SAA, i.e., by setting SAAMODE=STRICT and TENTACLE=YES when calling *nupipeline* to create Level 2 products. The background is stable with no strong flares in the lightcurve, so no further filtering has been adopted. The final effective exposure times are 181.49 ks (NE limb, telescope A), 180.95 ks (NE limb, telescope B), 188.37 ks (SW limb, telescope A), and 187.63 ks (NE limb, telescope B), respectively. Compared to a less strict setting of SAAMODE=OPTIMIZED, the resultant effective exposure time is $\sim 7\%$ shorter.

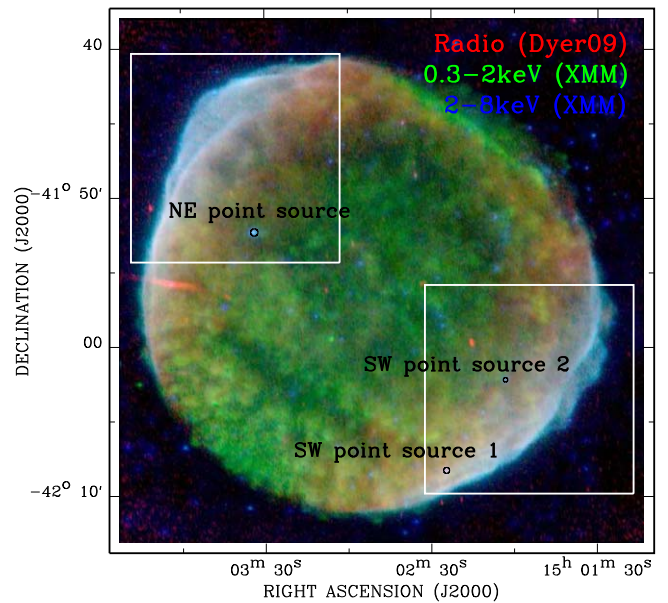


Figure 1. Tricolor images of SN1006—red: radio images from Dyer et al. (2009); green and blue: 0.3–2 keV and 2–8 keV *XMM-Newton* images from Li et al. (2015). The two white boxes roughly outline the FOV of the *NuSTAR* observations. The small black circles are the *XMM-Newton* spectral extraction regions of the three point sources detected by *NuSTAR* (Figures 2 and 4).

2.2. Background Analysis

We analyze the *NuSTAR* background using the software package *nuskybgd* (Wik et al. 2014). There are, in general, four major components of the *NuSTAR* background, which are discussed in detail in Wik et al. (2014). (1) Internal background $I_d(E)$. The internal background is comprised of two components: a featureless continuum plus various activation and fluorescence lines. The lines dominate the background in 22–32 keV, although some weaker lines are still present at higher energy. There is no significant spatial variation of the internal background across a given detector. (2) Aperture stray light $A_d(E, x, y)$. This component is caused by the “open” design of the telescope, so a fraction of the unfocused X-rays could strike the detectors. It is therefore expected that this “Aperture” background depends on the position (x, y) on the focal plane. The spectral shape, on the other hand, is consistent with the cosmic X-ray background (CXB). (3) Scattered and reflected stray light $S_d(E)$. This component is caused by the scattered and reflected X-rays from the entire sky (the CXB, the Earth, and the Sun) by different parts of the spacecraft (e.g., the mast). The scattered or reflected CXB emission could be directly added to the $A_d(E, x, y)$ component, while those from the Earth and the Sun are much softer and can be described with a thermal component (~ 1 keV; typically dominated below ~ 5 keV). Some weak fluorescence lines can be added to the $I_d(E)$ term. Therefore, the primary component of this $S_d(E)$ background is made up of the “Solar” emission and has no spatial variation. (4) Focused cosmic background $f_d(E, x, y)$. Like in other X-ray missions, the focused cosmic background (fCXB) is produced by unresolved foreground/background sources. This component is, in general, less important for *NuSTAR* and can only be noticeable below 15 keV. The fCXB background has some spatial variations, which depend on the direction of the observations.

For background analysis using *nuskybgd*, we first define a few (five) background regions (dashed boxes in Figure 2) for

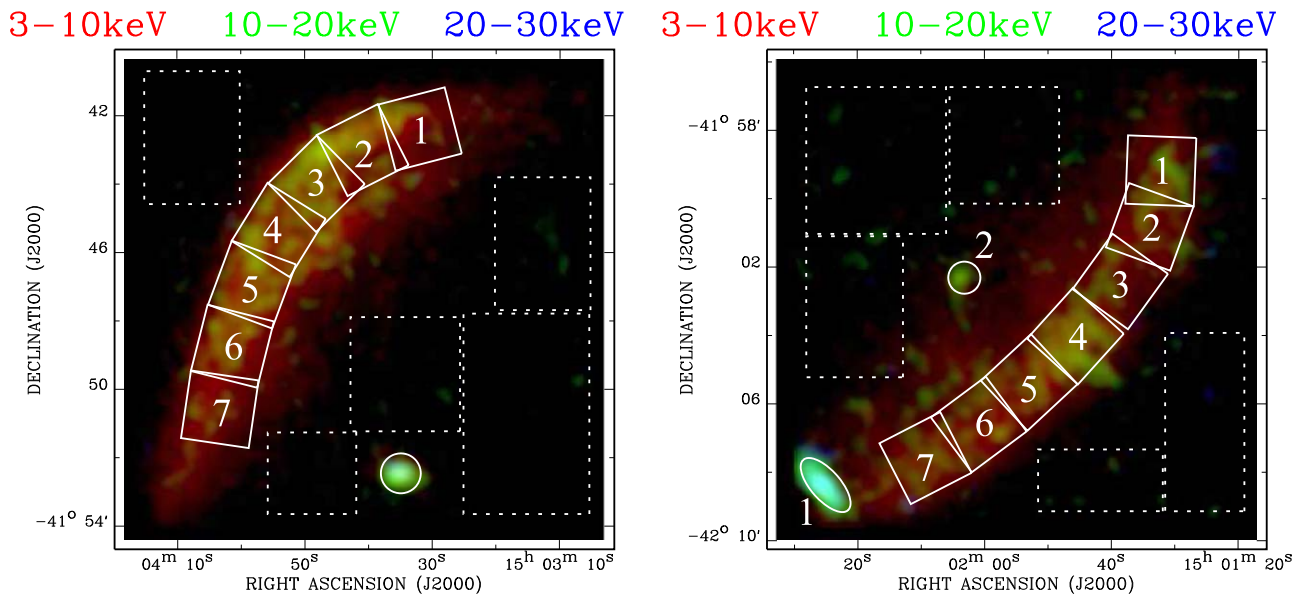


Figure 2. *NuSTAR* tricolor (red: 3–10 keV; green: 10–20 keV; blue: 20–30 keV) images of the NE and SW limbs from the two white boxes in Figure 1. Solid regions (boxes, circle, and ellipse) are used to extract source spectra, while dashed boxes are those used to extract background spectra. The box regions used to extract spectra from the two nonthermal limbs are labeled “1–7.” The two point-like sources in the FOV of the SW limb are also labeled “1” and “2.”

each field of view (FOV; for the NE and SW limbs), in order to sample the spatial variation of different background components. These background regions are known to have negligible nonthermal X-ray emission, although thermal emission typically $\lesssim 2$ keV does present in the SNR interior (Figure 1, e.g., Li et al. 2015, 2016). We then make instrument maps using the IDL tool `nuskybgd_instrmap` and create detector and background aperture images using `projinitbgds`. The background spectra are extracted using the PYTHON tool `getspecnoarf`. We then jointly fit the background spectra extracted from different regions using `nuskybgd_fitab`; this tool simultaneously creates background parameter files that will be used to create background images (using `nuskybgd_image`) and background spectra for a source region (Section 2.3). The above background analyses are conducted for the NE and SW FOVs separately. Examples of the fitted background spectra in the NE and SW FOVs are presented in Figure 3.

2.3. Spectral Analysis

For *NuSTAR* spectral analysis of extended sources, local sky backgrounds may not be accurate enough because they do not account for the spatial variation of some background components (Section 2.2). We therefore create simulated background spectra for each source region based on the background spectral parameters obtained in Section 2.2. This is achieved using the `nuskybgd` tool `nuskybgd_spec`. We also extract source spectra using the standard HEASOFT tool `nuproducts`.

The above spectra extraction is adopted for a few source regions as presented in Figure 2. Each source region is a $2' \times 2'$ box roughly along the nonthermal limbs. The size of the boxes is significantly larger than the FWHM (full width at half maximum; $18''$) or the HPD (half power diameter; $58''$) of *NuSTAR* (Harrison et al. 2013). Therefore, the spectra are not significantly affected by the spilling out photons in the PSF wing or the scattered light from surrounding regions. Below we

will discuss the modeling of the spectra extracted from various regions along the nonthermal limbs. The spectra of a few bright point-like sources will be presented in Section 2.4.

We jointly fit the *NuSTAR* spectra from this work, the *XMM-Newton* spectra from Li et al. (2015, 2016), and the 1.37 GHz radio flux measured from the flux-accurate image constructed with both the *VLA* and *GBT* data (Dyer et al. 2009) with the Interactive Spectral Interpretation System (ISIS; Houck & Denicola 2000). The spectra or flux in different bands are extracted from the same regions, which are significantly larger than the PSF of each observation. These multiwavelength spectra are fitted with various nonthermal emission models, with all the physical parameters linked and a constant scaling factor multiplied to each X-ray spectrum in order to account for small uncertainties in the normalization (caused by the bad pixels, CCD gaps, or the empty regions out of the FOV). We fix this constant at 1 for the *NuSTAR* telescope A and the radio flux, in order to make sure that the joint flux calibration is accurate and not biased by the scaling factor. The scaling factors of *NuSTAR* telescope B and the *XMM-Newton* spectra extracted from different instruments (MOS-1, MOS-2, PN) and different observations are all allowed to vary. The best-fit constants of different spectra are, in general, close to 1, ensuring the accuracy of the cross-flux calibration of different data.

2.4. Point-like Sources

There are three prominent hard X-ray bright point-like sources detected by the two *NuSTAR* observations, one in the NE FOV, the other two in the SW FOV (Figure 2). The apparently elongated morphology of the SW point source 1 is indeed consistent with the shape of the PSF at the corresponding location (An et al. 2014). All these three sources have soft X-ray counterparts detected by *XMM-Newton*, but only the one located in the NE FOV is significantly brighter than the soft X-ray knots of the SN ejecta (Figure 1). We cross-identify

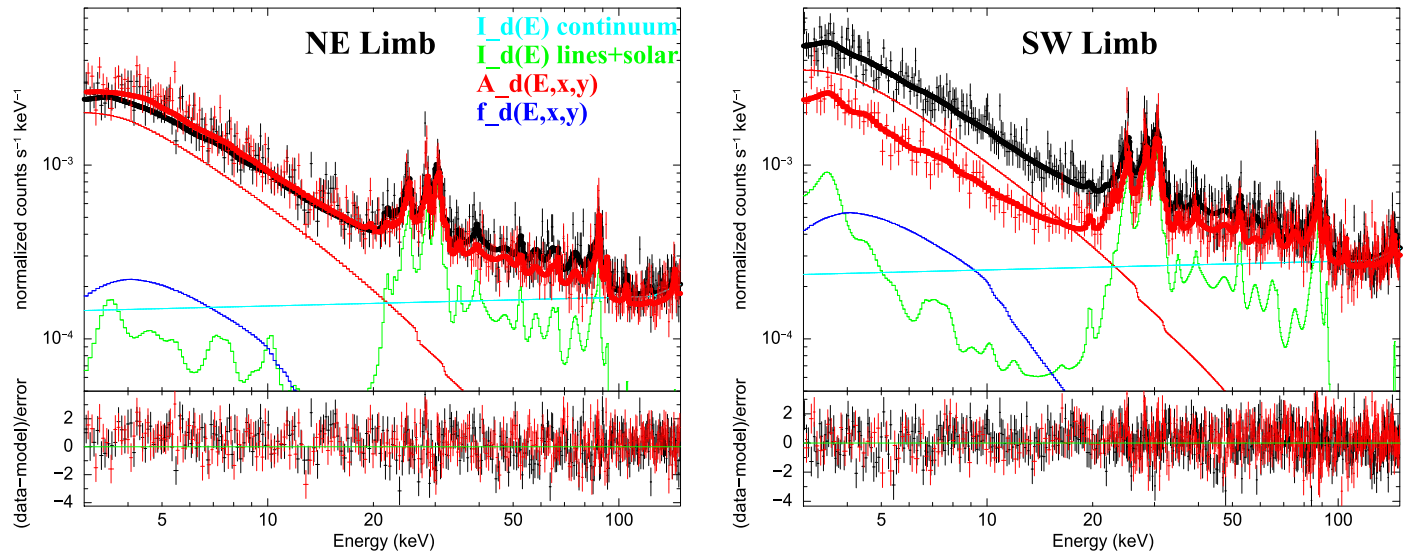


Figure 3. Background spectra of the NE (left) and SW (right) FOV. Black and red data points represent spectra extracted from telescopes A and B, respectively, but we only show an example of one of the five background regions in each FOV (dotted boxes in Figure 2). The spectra extracted from different regions, however, are jointly fitted in order to sample the spatial variation of different background components. There are basically four background components: Internal $I_d(E)$ (two component: a featureless continuum plus lines), Aperture Stray Light $A_d(E, x, y)$, Scattered and Reflected Stray Light $S_d(E)$ (“solar” and part of A_d), and Focused Cosmic Background $f_d(E, x, y)$ (Wik et al. 2014), which are plotted with thin curves in different colors. Background components with spatial variation are denoted with (x, y) . The thick solid curve is the sum of different background components (best-fit).

these three sources with online catalogs (such as SIMBAD, Wenger et al. 2000). Two sources, the NE source and the SW source 1, have multiwavelength counterparts and are both identified as background AGNs (Table 1). The third source, SW source 2, although it seems to have a very faint optical counterpart, is not identified in other catalogs.

These three sources all have harder X-ray spectra than the nonthermal limbs, so we have a few data points above 30 keV that are not too strongly affected by the instrumental lines (Figure 4). We extract *XMM-Newton* spectra from smaller regions than the *NuSTAR* spectral extraction regions (Figure 1), in order to avoid too much contribution from the thermal plasma in the surrounding area, which is not important in the *NuSTAR* band. We then need to multiply a scaling factor to account for this difference in area scale when jointly analyzing the *XMM-Newton* and *NuSTAR* spectra.

Selected parameters of the X-ray spectral models are summarized in Table 1. The *XMM-Newton* and *NuSTAR* spectra of the NE point source and SW point source 2 can both be well fitted with a single power law plus thermal (described with a NEI model) and background components (Figures 4(a), (c)). The power-law photon index of the SW point source 2 is consistent with those of X-ray binaries, and since it does not have a bright optical or IR counterpart, it is most likely a Galactic source. The SW point source 1 has much more complicated X-ray spectra, which include an additional Fe K line with a broadened low-energy wing (Figure 4(b)). This feature can be roughly fitted with a model describing the emission from the accretion disk of a supermassive black hole (“kerrdisk”; Brenneman & Reynolds 2006). Furthermore, the broadband nonthermal continuum cannot be fitted with a single power law, and a significant flattening of the spectra at $\gtrsim 3.2$ keV is clearly revealed by *NuSTAR*. This source has a near-IR counterpart that is a background galaxy (Table 1), so most likely to be the AGN of this galaxy.

Table 1
Parameters of the Point-like Sources Detected by *NuSTAR*

Name	NE	SW 1	SW 2
RA	15 ^h 03 ^m 34 ^s .1	15 ^h 02 ^m 24 ^s .9	15 ^h 02 ^m 03 ^s .5
DEC	−41 ^d 52 ^m 24 ^s .1	−42 ^d 08 ^m 24 ^s .4	−42 ^d 02 ^m 19 ^s .9
Identifier	QSOJ1503-4152	2MASXJ15022467-	...
		4208244	
Type	Quasar	Galaxy	...
Redshift	0.335	0.05388	...
d (")	1.23	2.46	...
Model	power+NEI	bknpower+kerr-disk+NEI	power+NEI
Γ_1	1.65 ± 0.02	$2.58^{+0.03}_{-0.04}$	1.82 ± 0.11
Γ_2	...	0.57 ± 0.02	...
E_{break}	...	$3.21^{+0.04}_{-0.05}$...
$spin_{XMM}$...	$0.024^{+0.001}_{-0.002}$...
$F_{0.5-3\text{keV}}$	0.48 ± 0.02	0.52 ± 0.01	0.16 ± 0.02
$F_{3-10\text{keV}}$	1.27 ± 0.06	1.99 ± 0.06	0.40 ± 0.03
$F_{10-30\text{keV}}$	1.73 ± 0.08	9.06 ± 0.28	0.45 ± 0.06
$F_{30-80\text{keV}}$	2.22 ± 0.12	$35.21^{+1.08}_{-1.90}$	$0.49^{+0.12}_{-0.10}$
$F_{\text{kerr},NuSTAR}$...	0.20 ± 0.05	...
$F_{\text{kerr},XMM}$...	$0.43^{+0.03}_{-0.01}$...

Note. The sources are cross-identified with SIMBAD (Wenger et al. 2000), with the closest identifier having a distance of d from the *NuSTAR* source. Γ_1 and Γ_2 are the photon indexes of the power-law or broken-power-law component. E_{break} is the break energy of the broken power law. Fluxes in different bands (in units of 10^{-13} erg s^{-1} cm^{-2}) are measured only for the power-law or broken-power-law component after removing the NEI component representing the plasma from the SNR and the background components. For the SW point source 1, we add another component (“kerrdisk”; Brenneman & Reynolds 2006) describing the broad Fe K line. As this line has significantly different strength in the *XMM-Newton* and *NuSTAR* spectra, we allow the parameters of this component to be different between the two sets of spectra. Since the Fe K line in the *NuSTAR* spectra is too weak, we only list the dimensionless black hole spin determined with the *XMM-Newton* data ($spin_{XMM}$). $F_{\text{kerr},NuSTAR}$ and $F_{\text{kerr},XMM}$ are the 3–10 keV fluxes (also in unit of 10^{-13} erg s^{-1} cm^{-2}) of the kerrdisk component of SW source 1 measured with the *NuSTAR* and *XMM-Newton* data, respectively.

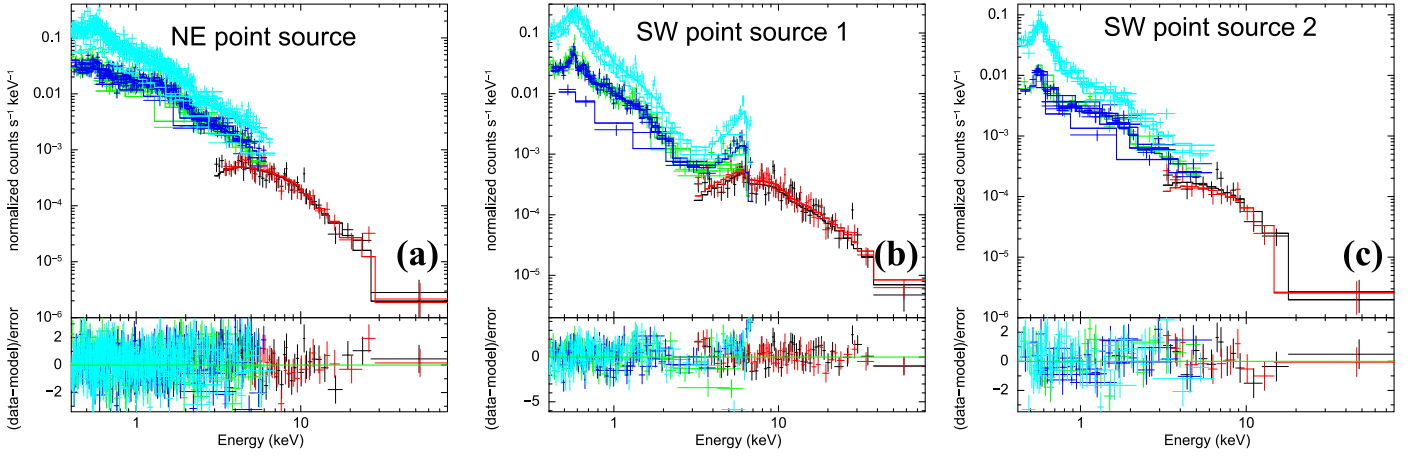


Figure 4. *NuSTAR* spectra (black: telescope A; red: telescope B) of the three most luminous point-like sources in the FOV (Figure 2). The spectra are fitted with a power law (a), (c) or broken power (b) plus a thermal plasma (NEI) and background components. The best-fit photon indexes of each source are also marked in the corresponding panel. An additional broadened Fe K line from the accretion disk of a supermassive black hole (kerrdisk) is also needed to fit the spectra of the SW point source 1 (b).

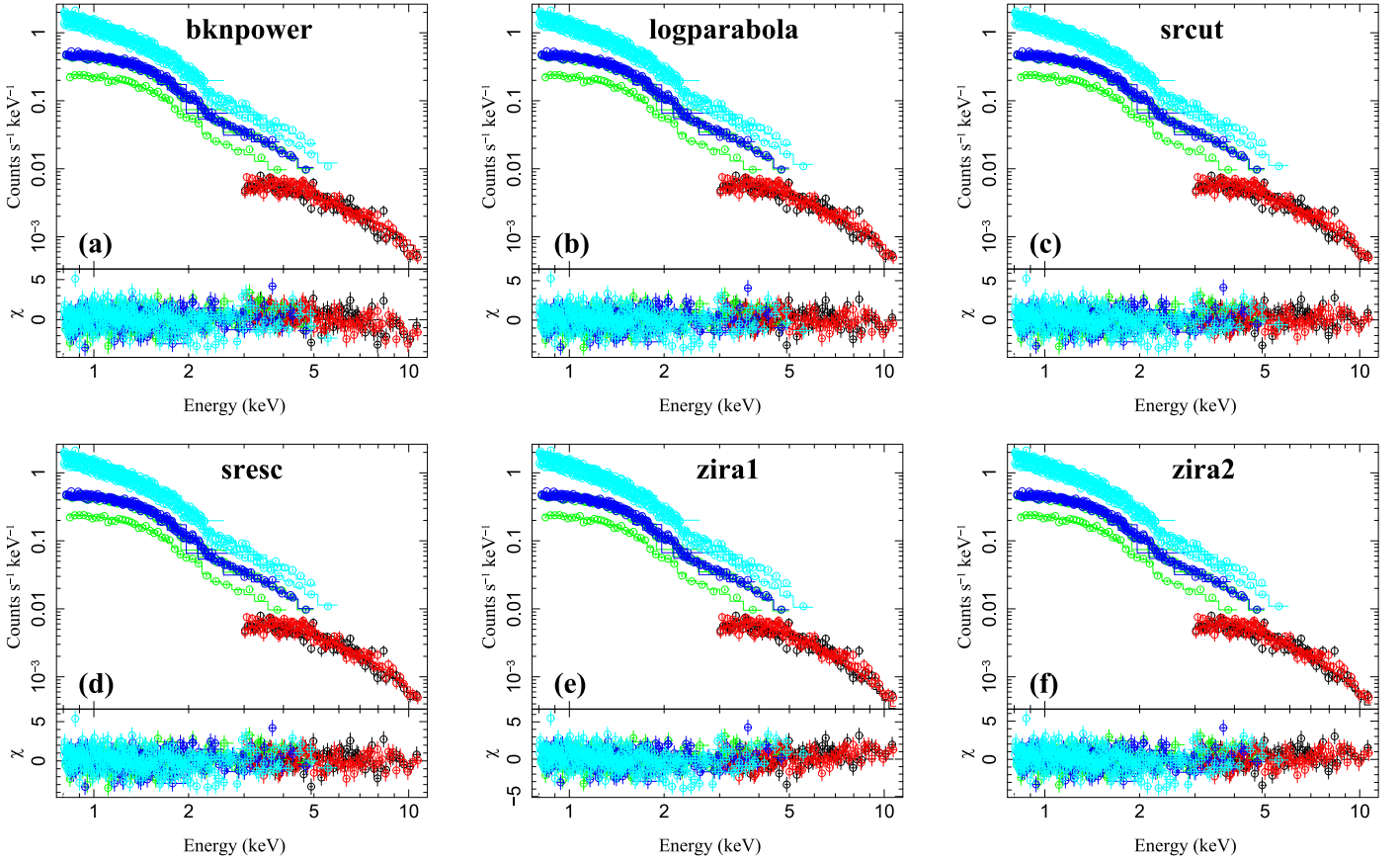


Figure 5. Example *NuSTAR* (black: telescope A; red: telescope B) and *XMM-Newton* (green: MOS-1; blue: MOS-2; cyan: PN; only data at >0.8 keV are included in the fit and plot) spectra of a source region “3” in the NE Limb (Figure 2). The spectra are fitted with different models: (a) broken power law; (b) log-parabolic; (c) srcut; (d) sresc; (e) zira1; (f) zira2, as described in the text. All these models are subject to foreground absorption (described with a “wabs” model) with the column density fixed in the direction of SN1006 ($N_{\text{H}} = 6.8 \times 10^{20} \text{ cm}^{-2}$; Dubner et al. 2002). Each spectrum (except for *NuSTAR* telescope A) is also renormalized by a scaling factor close to 1 in order to account for the small calibration bias. Best-fit parameters of different models are summarized in Tables 2–6. The complete figure set (14 images) for all regions is available in the online journal.

(The complete figure set (14 images) is available.)

Table 2
Best-fit Power-law Index in *NuSTAR* and *XMM-Newton* Bands

Region	Γ_{NuSTAR}	χ^2/dof	dof	Γ_{XMM}	χ^2/dof	dof
NE_1	$3.276^{+0.105}_{-0.102}$	1.116	91	2.677 ± 0.007	1.932	3002
NE_2	$3.011^{+0.069}_{-0.067}$	0.949	157	2.520 ± 0.006	1.643	3446
NE_3	$2.948^{+0.065}_{-0.064}$	1.140	175	2.495 ± 0.006	1.551	3524
NE_4	$3.099^{+0.070}_{-0.068}$	0.865	162	2.528 ± 0.006	1.492	3351
NE_5	$2.955^{+0.067}_{-0.065}$	1.174	170	2.503 ± 0.006	1.458	3627
NE_6	$3.211^{+0.077}_{-0.074}$	0.843	144	2.562 ± 0.006	1.533	3851
NE_7	$3.372^{+0.105}_{-0.101}$	1.096	100	2.675 ± 0.005	1.893	5043
SW_1	$2.978^{+0.122}_{-0.118}$	0.708	66	2.703 ± 0.008	2.069	3069
SW_2	$3.208^{+0.102}_{-0.098}$	0.815	84	2.646 ± 0.008	2.202	2879
SW_3	$3.134^{+0.112}_{-0.108}$	1.264	79	2.701 ± 0.010	2.105	2110
SW_4	$3.043^{+0.077}_{-0.074}$	0.815	136	2.664 ± 0.009	1.610	1720
SW_5	$3.158^{+0.078}_{-0.075}$	0.955	126	2.690 ± 0.009	1.380	1585
SW_6	$3.159^{+0.081}_{-0.078}$	0.822	114	2.694 ± 0.008	1.323	1705
SW_7	$3.118^{+0.090}_{-0.087}$	1.065	100	2.702 ± 0.008	1.326	1728

Note. Spectral extraction regions are presented in Figure 2. Γ_{NuSTAR} and Γ_{XMM} are the photon indexes obtained by fitting only the *NuSTAR* and *XMM-Newton* spectra, respectively. All the spectra have been rebinned to a signal-to-noise ratio of $\text{SNR} = 5$. The spectra are fitted after subtracting various background components (Section 2.2). Errors are quoted at the 1σ level.

Table 3
Best-fit Parameters of the Bknpower Model

Region	Γ_1	$E_{\text{break}}/\text{keV}$	Γ_2	χ^2/dof	dof
NE_1	$2.467^{+0.021}_{-0.023}$	$1.657^{+0.084}_{-0.087}$	$2.834^{+0.028}_{-0.026}$	1.777	706
NE_2	$2.389^{+0.024}_{-0.034}$	$2.093^{+0.370}_{-0.335}$	$2.705^{+0.087}_{-0.063}$	1.642	873
NE_3	$2.349^{+0.017}_{-0.019}$	$1.853^{+0.157}_{-0.121}$	$2.641^{+0.031}_{-0.027}$	1.583	854
NE_4	2.375 ± 0.015	$1.921^{+0.097}_{-0.093}$	$2.719^{+0.029}_{-0.026}$	1.375	826
NE_5	$2.359^{+0.013}_{-0.014}$	$2.064^{+0.122}_{-0.109}$	$2.711^{+0.037}_{-0.031}$	1.455	877
NE_6	$2.360^{+0.024}_{-0.025}$	$1.570^{+0.097}_{-0.084}$	$2.673^{+0.022}_{-0.020}$	1.500	919
NE_7	$2.515^{+0.012}_{-0.011}$	$1.890^{+0.073}_{-0.056}$	$2.861^{+0.026}_{-0.023}$	1.722	1053
SW_1	$2.449^{+0.030}_{-0.029}$	$1.408^{+0.070}_{-0.053}$	$2.802^{+0.025}_{-0.022}$	1.795	614
SW_2	2.373 ± 0.035	$1.436^{+0.096}_{-0.066}$	$2.763^{+0.031}_{-0.027}$	2.005	566
SW_3	$2.414^{+0.077}_{-0.039}$	$1.438^{+0.252}_{-0.069}$	$2.830^{+0.099}_{-0.033}$	1.904	400
SW_4	$2.551^{+0.016}_{-0.040}$	$2.327^{+0.204}_{-0.469}$	$2.947^{+0.067}_{-0.121}$	1.337	474
SW_5	2.518 ± 0.020	$1.829^{+0.099}_{-0.083}$	$2.896^{+0.034}_{-0.031}$	1.274	480
SW_6	2.577 ± 0.020	$2.166^{+0.259}_{-0.209}$	$2.942^{+0.076}_{-0.055}$	1.192	514
SW_7	$2.566^{+0.017}_{-0.018}$	$1.901^{+0.128}_{-0.085}$	$2.871^{+0.033}_{-0.028}$	1.273	513

Note. Parameters of the broken-power-law model (bknpower) obtained by jointly fitting the *NuSTAR* and *XMM-Newton* spectra (panel (a) of Figure 5). The *NuSTAR* spectra have been rebinned to a signal-to-noise ratio of $\text{SNR} = 5$, while the *XMM-Newton* spectra have been rebinned to a signal-to-noise ratio of $\text{SNR} = 20$. Γ_1 and Γ_2 are the photon indexes below and above the break energy E_{break} .

3. Results from Spectral Analysis

3.1. Curvature of Synchrotron X-Ray Spectra

We first use a few mathematical models to characterize the overall shape of the broadband nonthermal X-ray continuum from 0.8 keV to >10 keV (panels (a), (b) of Figure 5). We characterize the shape of the nonthermal spectra in three ways: (1) use two different power-law models to fit the *NuSTAR* and *XMM-Newton* spectra, respectively; use (2) a broken-power-law (“bknpower”) or (3) a curved-power-law model described with

Table 4
Best-fit Parameters of the Logparabola Model

Region	γ	β	χ^2/dof	dof
NE_1	2.408 ± 0.017	0.521 ± 0.038	1.657	707
NE_2	2.304 ± 0.015	$0.378^{+0.029}_{-0.028}$	1.524	874
NE_3	2.285 ± 0.016	$0.377^{+0.030}_{-0.029}$	1.479	855
NE_4	2.296 ± 0.016	$0.431^{+0.032}_{-0.030}$	1.267	827
NE_5	2.275 ± 0.015	$0.406^{+0.030}_{-0.029}$	1.386	878
NE_6	2.325 ± 0.015	$0.438^{+0.030}_{-0.029}$	1.361	920
NE_7	2.439 ± 0.014	$0.442^{+0.031}_{-0.030}$	1.681	1054
SW_1	2.460 ± 0.020	$0.502^{+0.051}_{-0.048}$	1.800	615
SW_2	2.368 ± 0.021	$0.572^{+0.051}_{-0.048}$	1.893	567
SW_3	2.419 ± 0.025	$0.573^{+0.063}_{-0.059}$	1.836	401
SW_4	2.455 ± 0.021	$0.392^{+0.043}_{-0.042}$	1.249	475
SW_5	2.458 ± 0.021	$0.444^{+0.042}_{-0.041}$	1.197	481
SW_6	2.489 ± 0.020	0.398 ± 0.039	1.101	515
SW_7	2.504 ± 0.019	$0.371^{+0.039}_{-0.038}$	1.207	514

Note. Similar to Table 3, but for the parameters of the log-parabolic model obtained by jointly fitting the *NuSTAR* and *XMM-Newton* spectra (panel (b) of Figure 5). γ is the power-law index, while β is the curvature. The reference energy x_{ref} is fixed at 1 keV (Section 3.1).

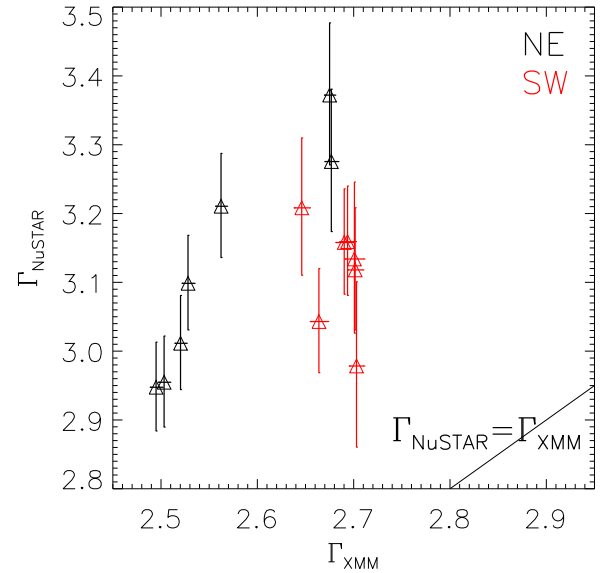


Figure 6. Photon indexes of the power-law fit to only the *XMM-Newton* (x-axis) or *NuSTAR* data (y-axis). Black and red data points are measurements from the NE and SW limb, respectively. The solid line is where $\Gamma_{\text{NuSTAR}} = \Gamma_{\text{XMM}}$. It is obvious that the spectra in the *NuSTAR* band are systematically steeper than those in the *XMM-Newton* band.

the formula $f(x) = \text{norm} \cdot (x/x_{\text{ref}})^{-\gamma - \beta \cdot \log_{10}(x/x_{\text{ref}})}$ (“logparabola,” where x_{ref} is fixed at 1 keV; Massaro et al. 2004) to jointly fit the *NuSTAR* and *XMM-Newton* spectra simultaneously.

We fit the spectra extracted from all the box regions in Figure 2 with these models and present the fitted spectra with the bknpower and log-parabolic models in panels (a) and (b) of Figure 5. The best-fit physical parameters, their 1σ errors, the reduced χ^2 , and degree of freedom (dof) of each region are summarized in Tables 2 (for the power-law model fitting the *NuSTAR* and *XMM-Newton* spectra, respectively), 3 (for the

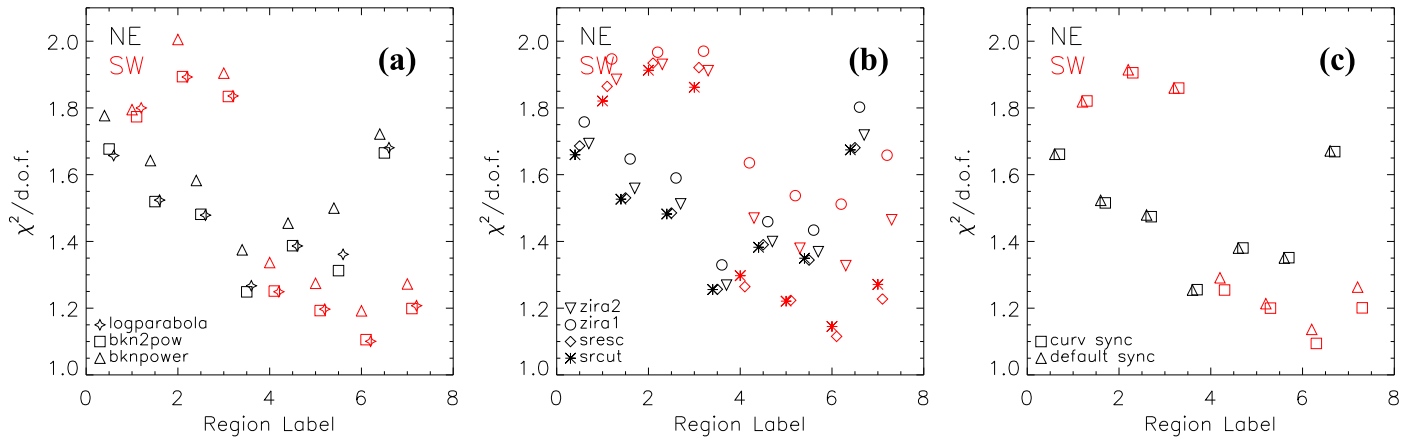


Figure 7. Reduced χ^2 of the fitted spectra of different regions. Different symbols represent reasonable fits with different models, as denoted in the lower left corner of each panel. Black and red colors represent regions on the NE and SW limbs, respectively. The x-axis is the region label as shown in Figure 2. Regions with the same label on the NE and SW limbs, as well as the fitting results with different models for the same region, are slightly shifted on the x-axis in order to be clearly separated. χ^2/dof of different models are summarized in Tables 2–7.

bknpower model), and 4 (for the log-parabolic model). In all these spectral analyses, we have adopted foreground absorption column density toward SN1006 (N_{H} fixed at $6.8 \times 10^{20} \text{ cm}^{-2}$; Dubner et al. 2002). The exact value of N_{H} does not affect the nonthermal X-ray emission at $\gtrsim 0.8 \text{ keV}$ significantly. We removed the data $\gtrsim 20 \text{ keV}$ in the *NuSTAR* spectra, where the synchrotron emission is too weak and the residual background from some strong emission lines at $\sim 20\text{--}30 \text{ keV}$ (Figure 3) make the spectra much more uncertain than those at lower energy. We also remove the data points at $\lesssim 0.8 \text{ keV}$ in the *XMM-Newton* spectra, where the strong oxygen emission lines from a thermal plasma component (much stronger than those in Figure 4) may affect the fitting of the pure nonthermal emission. We add the sky background models described in Li et al. (2015) to the *XMM-Newton* spectra, which are extracted from an annulus out of the SNR and have been rescaled to each region according to their effective sky area.

In the joint analyses of the spectra with significantly different counting statistics, such as the *XMM-Newton* and *NuSTAR* spectra of SN1006, the χ^2/dof may not accurately reflect the goodness of the fit in a certain band. As we are more interested in the high energy band poorly constrained in previous observations (typically at $\gtrsim 7 \text{ keV}$), we justify the goodness of the model not only by the χ^2/dof for the whole spectra, but also by the presence of any systematical departure of the data from the “best-fit” model. Furthermore, we also regroup the *NuSTAR* and *XMM-Newton* spectra with different signal-to-noise ratios ($S/N=5$ for *NuSTAR* and $S/N=20$ for *XMM-Newton*), so that there will not be too many *XMM-Newton* data points compared to the relatively few *NuSTAR* data points. The goodness of the fit in the *NuSTAR* band could then be reflected by the relatively small change of the χ^2/dof in the fitting process.

The spectral slope in the *NuSTAR* band ($\Gamma_{\text{NuSTAR}} \sim 2.9\text{--}3.4$; typically from 3 keV to $\sim 15 \text{ keV}$) is systematically steeper than those in the *XMM-Newton* band ($\Gamma_{\text{XMM}} \sim 2.5\text{--}2.7$; typically 0.8–7 keV; Table 2). This systematical bias indicates a significant curvature of the broadband nonthermal X-ray emission spectra. There seems to be a positive correlation between Γ_{NuSTAR} and Γ_{XMM} for the NE limb, but all regions in the SW limb are compatible with the same spectral slope in both *NuSTAR* and *XMM-Newton* bands (Figure 6).

In most of the cases, the log-parabolic model fits the broadband X-ray spectra better than a bknpower model (Tables 3 and 4, Figure 7(a)), with the bknpower model tends to overpredict the X-ray emission at $\gtrsim 8 \text{ keV}$ (e.g., Figure 5(a)). This indicates that the broadband synchrotron emission is curved and more complicated than a broken power law with a single break.

3.2. Loss- and Escape-limited Models in the X-Ray Band

We next examine some physical synchrotron emission models in the fitting of the broadband X-ray spectra, assuming all the synchrotron emissions are produced by a single population of CR electrons. We have adopted four loss- or escape-limited models all with two free parameters: (1, 2) The synchrotron spectrum described in Reynolds (1998), from either an exponentially cutoff power-law distribution of electrons in a homogeneous magnetic field (“srcut”), or an electron distribution limited by particle escape above a break energy (“sresc”). We caution that these two models may be oversimplified with the homogeneous magnetic field assumption, as the spatial variation of the magnetic field in the upstream may change the shape of the synchrotron spectrum in the cutoff region. (3, 4) The loss-limited models described in Zirakashvili & Aharonian (2007). We adopt the two analytical forms described in Miceli et al. (2013), with slightly different parameters depending on whether the magnetic field downstream is compressed by a factor $\kappa = \sqrt{11}$ (“zira2”) or not (“zira1”) with respect to upstream. We have fixed the normalization of the srcut and sresc models at the radio flux extracted from the flux-accurate image of Dyer et al. (2009), so all these four models have just two free physical parameters (plus a constant scaling factor of each spectra that is ≈ 1 , except for *NuSTAR* telescope A): the radio spectral index α and cutoff frequency ν_{cutoff} (converted to energy unit E_{cutoff} for the convenience of comparison) of srcut and sresc, and the cutoff energy (E_{cut}) and normalization of zira1 and zira2. The best-fit spectra are presented in panels (c)–(f) of Figure 5, while the model parameters are listed in Tables 5 and 6.

In most of the regions, the srcut, sresc, and zira2 models fit the broadband nonthermal X-ray spectra almost equally well, and slightly better than the zira1 model (Figure 7(b)), which usually tends to underpredict the X-ray emission at

Table 5
Best-fit Parameters of the Srcut and Sresc Models

Region	α (srcut)	$E_{\text{cutoff}}/\text{keV}$ (srcut)	χ^2/dof (srcut)	α (sresc)	$E_{\text{cutoff}}/\text{keV}$ (sresc)	χ^2/dof (sresc)	dof
NE_1	0.458 ± 0.003	0.199 ± 0.005	1.660	0.491 ± 0.003	0.854 ± 0.024	1.686	708
NE_2	0.474 ± 0.002	0.321 ± 0.008	1.527	0.504 ± 0.002	$1.350^{+0.032}_{-0.030}$	1.530	875
NE_3	$0.479^{+0.003}_{-0.002}$	$0.342^{+0.009}_{-0.008}$	1.482	0.508 ± 0.002	$1.444^{+0.034}_{-0.033}$	1.485	856
NE_4	0.468 ± 0.003	$0.301^{+0.008}_{-0.007}$	1.256	0.499 ± 0.002	$1.287^{+0.030}_{-0.029}$	1.257	828
NE_5	0.471 ± 0.003	$0.331^{+0.009}_{-0.008}$	1.382	0.501 ± 0.002	$1.410^{+0.033}_{-0.030}$	1.390	879
NE_6	$0.470^{+0.003}_{-0.002}$	$0.276^{+0.007}_{-0.006}$	1.350	0.502 ± 0.002	$1.186^{+0.027}_{-0.026}$	1.344	921
NE_7	0.465 ± 0.003	$0.203^{+0.005}_{-0.004}$	1.674	0.497 ± 0.003	0.861 ± 0.021	1.681	1055
SW_1	0.447 ± 0.004	0.173 ± 0.005	1.821	0.478 ± 0.005	$0.722^{+0.032}_{-0.034}$	1.865	616
SW_2	0.462 ± 0.004	0.212 ± 0.007	1.913	$0.498^{+0.004}_{-0.003}$	$0.944^{+0.032}_{-0.030}$	1.934	568
SW_3	0.467 ± 0.004	0.189 ± 0.008	1.862	0.501 ± 0.005	0.829 ± 0.046	1.921	402
SW_4	0.473 ± 0.003	$0.213^{+0.007}_{-0.006}$	1.297	0.504 ± 0.003	$0.908^{+0.032}_{-0.030}$	1.264	476
SW_5	0.476 ± 0.003	$0.201^{+0.007}_{-0.006}$	1.221	0.507 ± 0.003	$0.841^{+0.031}_{-0.029}$	1.224	482
SW_6	0.467 ± 0.003	$0.191^{+0.006}_{-0.005}$	1.145	0.498 ± 0.004	$0.810^{+0.029}_{-0.030}$	1.115	516
SW_7	0.467 ± 0.003	0.190 ± 0.005	1.271	0.496 ± 0.004	$0.786^{+0.030}_{-0.029}$	1.228	515

Note. Similar to Table 3, but for the parameters of the srcut and sresc models obtained by jointly fitting the *NuSTAR* and *XMM-Newton* spectra (panels (c) and (d) of Figure 5). α is the radio spectral index, while E_{cutoff} is the cutoff energy of the photon spectra.

Table 6
Best-fit Parameters of the Zira1 and Zira2 Models

Region	$E_{\text{cut}}/\text{keV}$ (zira1)	χ^2/dof	$E_{\text{cut}}/\text{keV}$ (zira2)	χ^2/dof	dof
NE_1	0.192 ± 0.003	1.758	0.248 ± 0.004	1.693	708
NE_2	$0.279^{+0.005}_{-0.004}$	1.647	0.373 ± 0.007	1.559	875
NE_3	0.291 ± 0.005	1.590	0.392 ± 0.008	1.513	856
NE_4	$0.266^{+0.005}_{-0.004}$	1.330	0.355 ± 0.007	1.269	828
NE_5	0.287 ± 0.005	1.459	$0.387^{+0.008}_{-0.007}$	1.400	879
NE_6	0.247 ± 0.004	1.434	$0.327^{+0.006}_{-0.005}$	1.369	921
NE_7	0.193 ± 0.002	1.802	$0.249^{+0.004}_{-0.003}$	1.719	1055
SW_1	0.173 ± 0.003	1.947	0.222 ± 0.004	1.886	616
SW_2	0.197 ± 0.004	1.967	$0.256^{+0.006}_{-0.005}$	1.931	568
SW_3	0.179 ± 0.004	1.970	0.231 ± 0.006	1.912	402
SW_4	0.202 ± 0.004	1.635	0.259 ± 0.006	1.470	476
SW_5	$0.192^{+0.004}_{-0.003}$	1.537	0.245 ± 0.005	1.380	482
SW_6	0.189 ± 0.003	1.512	$0.241^{+0.005}_{-0.004}$	1.327	516
SW_7	0.188 ± 0.003	1.658	$0.239^{+0.005}_{-0.004}$	1.465	515

Note. Similar to Table 3, but for the parameters of the loss-limited models (zira1 and zira2) obtained by jointly fitting the *NuSTAR* and *XMM-Newton* spectra (panels (e) and (f) of Figure 5). E_{cut} is the cutoff energy of the synchrotron emission spectrum.

$kT \gtrsim 8$ keV (Figure 5(e)). But, in a few regions (SW 4–7), neither of the two loss-limited models (zira1 and zira2) could fit the spectra as well as the srcut and sresc models. The results are apparently inconsistent with Miceli et al. (2013), who found that the loss-limited models always give better fits to the *XMM-Newton* spectra than the escape-limited models. The spectral extraction regions adopted in the present paper are much larger than those adopted in Miceli et al. (2013) because of the much lower angular resolution of *NuSTAR*. Since Miceli et al. (2013) focus on the brightest nonthermal filaments, we may conclude that synchrotron radiative loss is only important in the X-ray band in limiting the particle acceleration at the brightest filaments.

3.3. Curvature of the Electron Energy Spectrum

We further examine if the broadband nonthermal emission from radio to hard X-ray can be described with the synchrotron emission of the same CR electron population. In order to fit the *NuSTAR* and *XMM-Newton* X-ray spectra together with the

radio flux extracted from the flux-accurate image of Dyer et al. (2009), we adopt the default built-in electron PDF of the nonthermal module of ISIS, which is responsible for the synchrotron emission from radio to X-ray (Allen et al. 2008). The PDF has the form of

$$dn/dp = A(p/p_0)^{f(p,a)} e^{-(p-p_0)/p_{\text{cutoff}}}, \quad (1)$$

where the index $f(p, a)$ is

$$f(p, a) = -\Gamma + a \times \log(p/p_0), \quad \text{when } p > p_0$$

$$f(p, a) = -\Gamma, \quad \text{when } p \leq p_0.$$

In Equation (1), n is the electron number density, $p = \gamma mv$ (γ , m , and v are the Lorentz factor, rest mass, and velocity of the particle), A is the normalization of the PDF in units of $p_0^{-1} \text{ cm}^{-3}$, $p_0 = 1 \text{ GeV } c^{-1}$, where c is the light speed, p_{cutoff} is the cutoff momentum, Γ and a characterize the slope and curvature of the PDF, respectively.

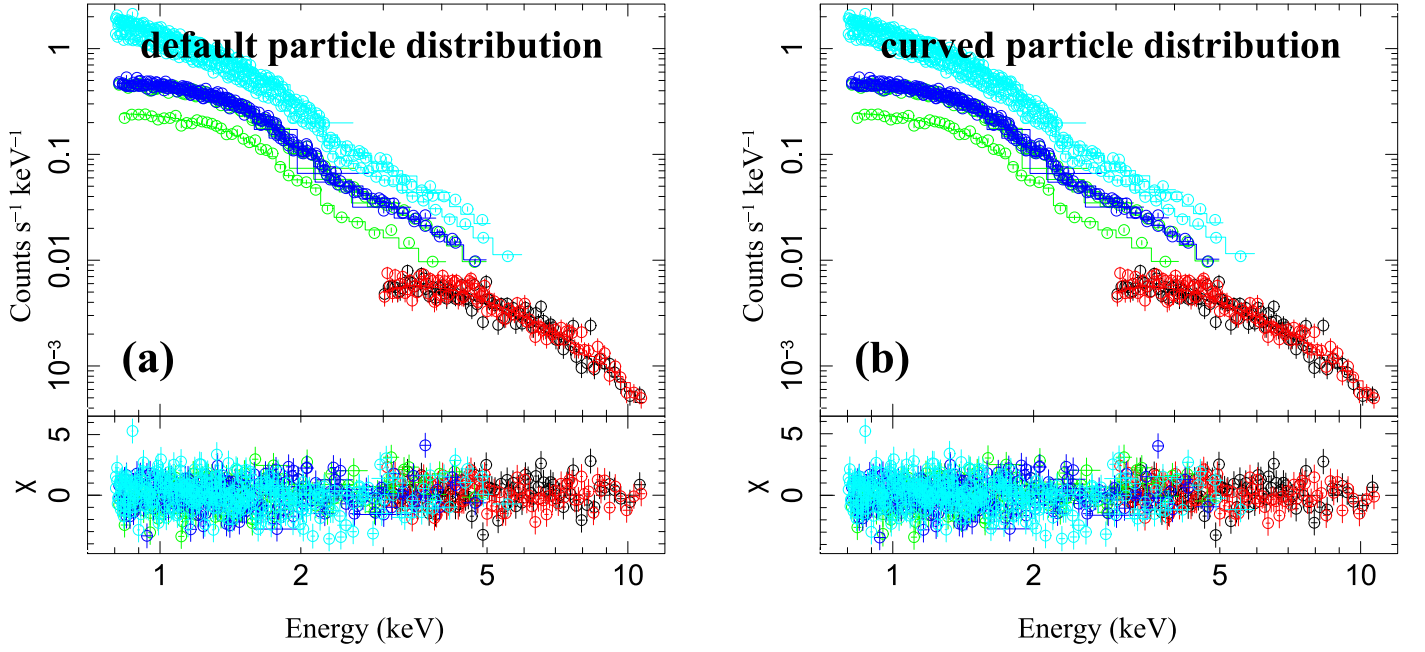


Figure 8. Similar to Figure 5, but in this figure the spectra from X-ray (*NuSTAR* and *XMM-Newton*) and radio (only one data point at 1.37 GHz, which is always well fitted) are jointly fitted with a synchrotron emission model of a power-law distribution of electron energy with an exponential cutoff (“default particle distribution”). Only X-ray spectra are presented for clarity. In panel (b), we further add a free parameter of curvature to the power-law distribution of electron energy (“curved particle distribution”). Best-fit parameters are summarized in Table 7.

Table 7
Best-fit Parameters of the Synchrotron Model with Exponentially Cutoff Power Law (Default) or Curved Particle Distributions

Region	Γ (default)	$E_{\text{cutoff}}/\text{TeV}$ (default)	χ^2/dof	dof	Γ (curved)	a (curved)	$E_{\text{cutoff}}/\text{TeV}$ (curved)	χ^2/dof	dof
NE_1	$1.899^{+0.020}_{-0.023}$	$5.93^{+0.09}_{-0.10}$	1.661	708	$2.095^{+0.278}_{-0.263}$	$0.052^{+0.075}_{-0.073}$	$5.39^{+0.73}_{-0.62}$	1.661	707
NE_2	$1.940^{+0.019}_{-0.021}$	7.56 ± 0.12	1.523	875	$1.607^{+0.193}_{-0.186}$	$-0.086^{+0.049}_{-0.046}$	$9.37^{+1.33}_{-1.10}$	1.515	874
NE_3	$1.950^{+0.019}_{-0.021}$	7.81 ± 0.13	1.479	856	$1.658^{+0.202}_{-0.194}$	$-0.075^{+0.052}_{-0.048}$	$9.46^{+1.42}_{-1.17}$	1.474	855
NE_4	$1.924^{+0.019}_{-0.022}$	7.31 ± 0.12	1.254	828	$1.891^{+0.219}_{-0.210}$	$-0.009^{+0.057}_{-0.053}$	$7.46^{+1.00}_{-0.84}$	1.255	827
NE_5	$1.931^{+0.019}_{-0.022}$	7.68 ± 0.12	1.380	879	$1.817^{+0.207}_{-0.198}$	$-0.030^{+0.054}_{-0.050}$	$8.24^{+1.12}_{-0.94}$	1.380	878
NE_6	$1.929^{+0.019}_{-0.022}$	$7.01^{+0.10}_{-0.11}$	1.350	921	$1.891^{+0.211}_{-0.203}$	$-0.010^{+0.055}_{-0.051}$	$7.17^{+0.90}_{-0.76}$	1.351	920
NE_7	$1.919^{+0.019}_{-0.022}$	6.00 ± 0.08	1.671	1055	$1.661^{+0.219}_{-0.213}$	$-0.067^{+0.057}_{-0.054}$	$6.90^{+0.90}_{-0.76}$	1.669	1054
SW_1	$1.878^{+0.021}_{-0.023}$	$5.57^{+0.09}_{-0.10}$	1.818	616	$1.775^{+0.366}_{-0.347}$	$-0.027^{+0.098}_{-0.089}$	$5.87^{+1.22}_{-0.93}$	1.821	615
SW_2	$1.907^{+0.021}_{-0.024}$	6.12 ± 0.11	1.914	568	$2.458^{+0.366}_{-0.341}$	$0.147^{+0.095}_{-0.091}$	$4.69^{+0.79}_{-0.64}$	1.905	567
SW_3	$1.918^{+0.021}_{-0.024}$	$5.78^{+0.13}_{-0.12}$	1.860	402	$2.260^{+0.437}_{-0.407}$	$0.091^{+0.117}_{-0.106}$	$4.89^{+1.06}_{-0.81}$	1.860	401
SW_4	$1.935^{+0.019}_{-0.022}$	6.12 ± 0.11	1.291	476	$1.199^{+0.277}_{-0.199}$	$-0.190^{+0.071}_{-0.053}$	$9.66^{+1.95}_{-1.63}$	1.254	475
SW_5	$1.942^{+0.020}_{-0.022}$	5.95 ± 0.10	1.213	482	$1.483^{+0.276}_{-0.264}$	$-0.119^{+0.072}_{-0.065}$	$7.69^{+1.41}_{-1.12}$	1.200	481
SW_6	$1.924^{+0.019}_{-0.021}$	$5.83^{+0.10}_{-0.09}$	1.136	516	$1.171^{+0.256}_{-0.171}$	$-0.194^{+0.065}_{-0.046}$	$9.09^{+1.50}_{-1.36}$	1.094	515
SW_7	$1.925^{+0.019}_{-0.021}$	5.82 ± 0.09	1.263	515	$1.021^{+0.260}_{-0.021}$	$-0.232^{+0.063}_{-0.010}$	$10.13^{+0.59}_{-1.61}$	1.201	514

Note. Parameters of the synchrotron emission model with exponentially cutoff power law (default) or curved particle distributions obtained by jointly fitting the X-ray (*NuSTAR* and *XMM-Newton*) and radio data (an example of the best-fit spectra are presented in Figure 8). Γ is the index of the power-law particle distribution function, E_{cutoff} is the exponential cutoff energy of the particle distribution function corresponding to the cutoff momentum p_{cutoff} , a is an additional parameter describing the curvature of the particle distribution function (Equation (1)). The magnetic field has been fixed at $100 \mu\text{G}$ because it is directly linked to E_{cutoff} .

We fit the broadband radio-X-ray spectrum with a synchrotron emission model of a population of CR electrons with a PDF described by Equation (1). For a given spectrum, the total magnetic field strength (B_{tot}) in the synchrotron emission model and the cutoff momentum in the PDF (p_{cutoff}) are not independent (e.g., Allen et al. 2008). We therefore need to fix one of them. There are, in general, two components of the magnetic field in SN1006: a large-scale ordered Galactic component along the SW–NE direction or roughly parallel to the Galactic plane (so the nonthermal limbs have a polar cap geometry) and a highly disordered and turbulent component at the two nonthermal limbs, which is likely responsible for the

particle acceleration (Reynoso et al. 2013). The strength of the disordered component in the post-shock region is poorly constrained from multiwavelength observations (e.g., Allen et al. 2001; Dyer et al. 2001; Aharonian et al. 2005), but is, in general, $\sim 100 \mu\text{G}$ based on recent estimates with various methods, such as the thickness of the shock compressed filaments or the broadband spectral analysis (e.g., Parizot et al. 2006; Acero et al. 2010; Morlino et al. 2010; Berezhko et al. 2012; Helder et al. 2012). We therefore arbitrarily fix B_{tot} at $100 \mu\text{G}$ in our analysis. We examine two sets of models, with or without a curvature in the PDF (i.e., $a = 0$ or set free, named as “default” or “curved”). An example of the best-fit

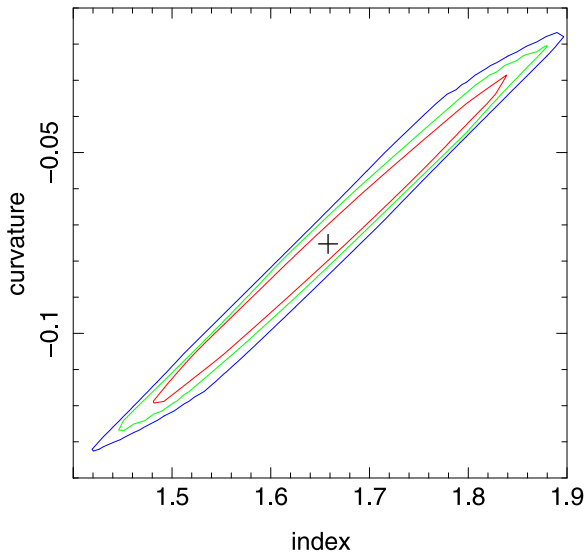


Figure 9. Confidence contours of the index (Γ) and curvature (a) of the curved PDF (Equation (1)) of NE region 3 (Figure 8(b)). Contours from inner to outer are at 1σ (68.3%; red), 1.64σ (90%; green), and 3σ (99.73%; blue) confidence levels.

spectra (only X-ray spectra are presented for clarity, the 1.37 GHz radio flux is always well fitted) are presented in Figure 8 and the best-fit model parameters are listed in Table 7. Because the best-fit spectra are very similar to those fitted with an *srcut* model, we do not present fitted spectra of other regions.

The radio flux and X-ray spectra can both be well fitted with such a synchrotron emission model simultaneously, indicating that they are produced by a single CR electron population. In most of the regions, the synchrotron emission of a curved or default PDF fit the spectra equally well (Figure 7(c)). We also found a tight correlation of the best-fit curvature and index of the PDF (Figure 9), and the curvature is very close to zero. Therefore, we do not find strong evidence of a curved PDF in the $2' \times 2'$ spectral extraction regions on the nonthermal limbs of SN1006, which has been claimed for smaller regions based on the radio spectra and higher-resolution *Chandra* data at $\lesssim 7$ keV (Allen et al. 2008). However, cautions need to be made that since we only have radio flux measurement at one frequency, there is no constraint on the radio spectral slope. Furthermore, the spectral slope obtained in *srcut* or *sresc* models ($\lesssim 0.5$) is always flatter than the average radio spectral index over the entire SNR (≈ 0.6 , e.g., Dyer et al. 2001; Rothenflug et al. 2004; Allen et al. 2008). This may explain the difference between our results and what has been found by Allen et al. (2008). Accurate and high-resolution flux measurements at a few different frequencies in the GHz band are needed to better characterize the broadband synchrotron spectrum in SN1006.

4. Discussions

4.1. Shape of the Broadband Synchrotron Emission and CR Energy Distribution

Standard diffusive shock acceleration (DSA) theory predicts the index of the energy spectrum of the accelerated particles to be $\Gamma = 2$ with a shock compression ratio of $r = 4$ (e.g., Blandford & Eichler 1987). In recent years, it has been noticed

that CRs could not be simply regarded as test particles, but must carry non-negligible amounts of energy and pressure and actively participate in the shock dynamics (e.g., Blandford & Eichler 1987; Caprioli 2012). Such nonlinear theories of DSA predict the back-reaction of the accelerated particles that form a precursor in the upstream and slow down the fluid. The net effect is that higher energy particles “feel” a larger compression ratio and are accelerated more efficiently. The resultant PDF is thus concave, with an index $\Gamma > 2$ at low energy and $\Gamma < 2$ at high energy.

Such a concavity in the PDF has not yet been clearly evidenced at a high confidence level. Allen et al. (2008) made use of the radio and *Chandra* X-ray observations of SN1006 and found that the synchrotron spectrum extracted from much smaller regions than those adopted in the present paper seem to flatten with increasing energy. For comparison, we have obtained an index of the “default” PDF for the NE limb typically in the range of 1.9–1.95 with a mean value of $\Gamma = 1.927^{+0.007}_{-0.008}$ ($\Gamma = 1.919^{+0.008}_{-0.009}$ for the SW limb; 1σ confidence; Table 7), which is even lower than the value of $\Gamma = 2.073^{+0.021}_{-0.020}$ (90% confidence) obtained from the *Chandra* and radio data also for the NE limb by Allen et al. (2008). This is probably because we have included the higher energy *NuSTAR* data in the analysis that makes the CR energy spectra even flatter. Γ in all of the regions based on the “default” PDF is also lower than the expected value (2.0) from the standard DSA. These flat synchrotron spectra are apparently consistent with the above scenario of nonlinear DSA, but we do not find a significant concavity of the PDF as claimed by Allen et al. (2008). Oppositely, the synchrotron emission spectrum shows significant curvature as indicated by the mathematical models in Section 3.1. Nevertheless, the scatter of the curvature a of the PDF in Equation (1) is too large and on average either negative, or more conservatively to say, not inconsistent with no curvature (the mean value for the NE/SW limb is $a = -0.032^{+0.022}_{-0.020}/a = -0.075^{+0.032}_{-0.027}$ at 1σ confidence compared to Allen et al.’s (2008) value of 0.054 ± 0.006 at 90% confidence for the NE limb; Figure 12(c), Table 7). Furthermore, we also find a strong dependence of a on the index Γ of the PDF (Figure 9), suggesting that we cannot simultaneously well constrain these two parameters with the current radio/X-ray spectra. Since the “default” PDF can fit the data equally well as the “curved” PDF, we conclude that the apparently curved synchrotron emission is a natural result of the synchrotron emission of an exponentially cutoff PDF with no significant concavity or curvature.

Miceli et al. (2013) analyzed the same *XMM-Newton* data set as adopted in the present paper, but extracted spectra from some smaller regions covering the brightest filaments in the nonthermal limbs. They found that the loss-limited models (*zira1* and *zira2*), in general, give better fits to the *XMM-Newton* spectra than the *srcut* model. This is good evidence for efficient synchrotron radiative loss that may change the shape of the nonthermal spectrum, at least in the brightest filaments. However, we do not obtain the same result, as the *srcut* (or *sresc*) model always gives a slightly better fit to the X-ray (*XMM-Newton* and *NuSTAR*) spectra than the loss-limited models (Figure 7(b)). This is probably because we have extracted spectra from larger regions, including those with less efficient synchrotron loss. Alternatively, a stronger nonlinear effect at higher energy (*NuSTAR* band) may flatten the synchrotron spectrum, and make the loss-limited

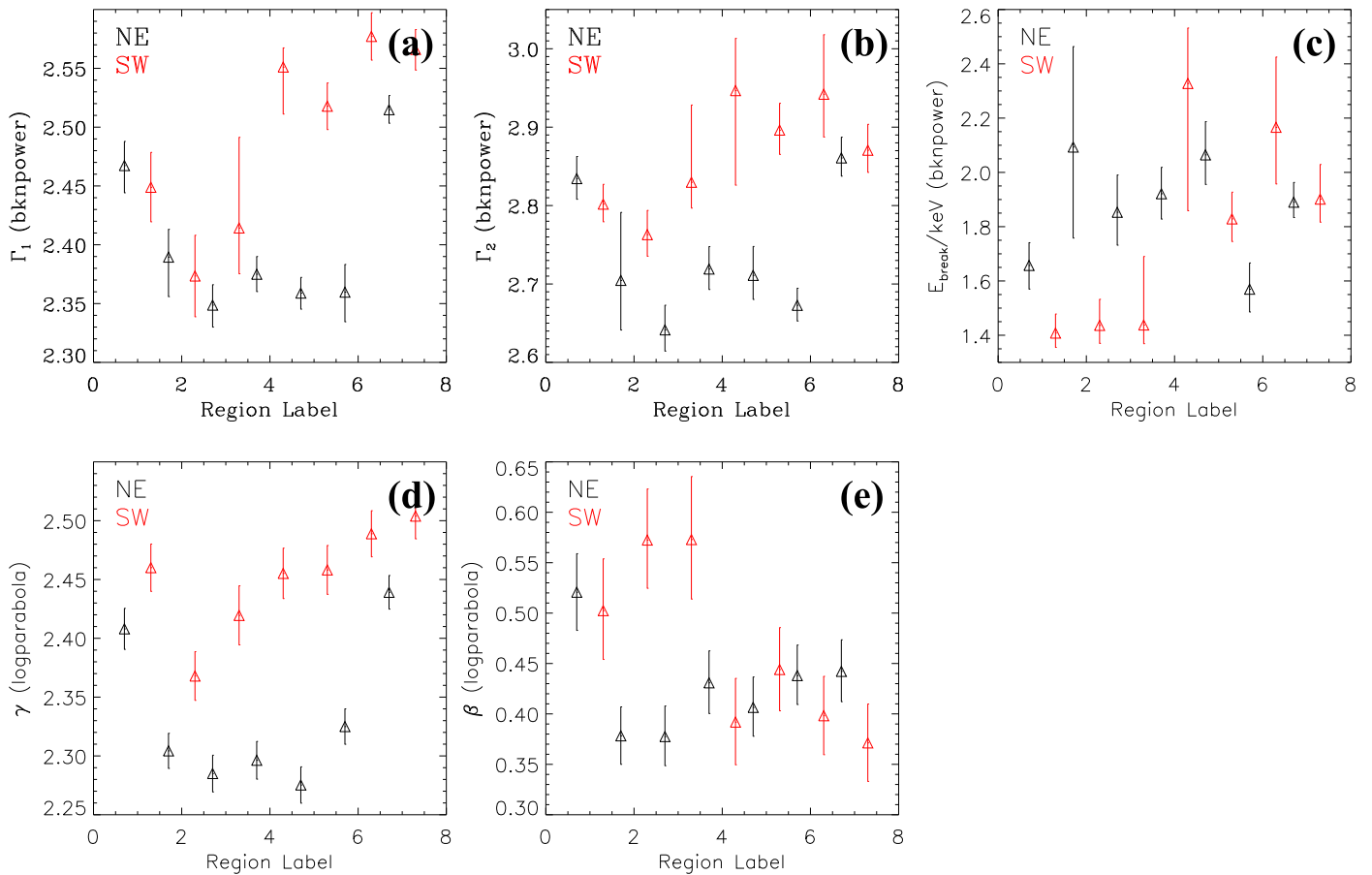


Figure 10. Azimuthal variation of the parameters of the mathematical models fitted to only the X-ray (*NuSTAR* and *XMM-Newton*) spectra. The top row shows the parameters of the broken power law, while the bottom row shows the parameters of the log-parabolic model. The best-fit spectra are presented in panels (a)–(b) of Figure 5, while the model parameters are listed in Tables 3 and 4.

models underpredict the synchrotron emission at high energy (the (e) and (f) panels of Figure 5).

The shape of the PDF can be affected by many processes. As discussed above, the nonlinear DSA tends to produce a concave PDF with $a > 0$, inconsistent with our observed value of $a \lesssim 0$. However, other processes may mitigate or even remove the curvature. These processes include, but are not limited to, efficient synchrotron radiative cooling at high energy (e.g., Zirakashvili & Aharonian 2007), density inhomogeneities in the downstream (e.g., Fraschetti et al. 2018), turbulent heating in the CR precursor (e.g., Berezhko & Ellison 1999), and enhanced magnetic field amplification induced by CR streaming in the upstream and the corresponding reduced compressibility of the plasma (e.g., Caprioli et al. 2009; Caprioli 2011).

4.2. Spatial Variation of Nonthermal Emission Parameters

We present the azimuthal variation of various spectral model parameters along the nonthermal limbs in Figures 10–12. The mathematical models indicate that the nonthermal spectrum is, in general, flatter (smaller photon index Γ for bknpower and γ for logparabola) in the center of the NE limb (region 4) and becomes steeper at larger azimuthal angles (from 4 to 1 or 4 to 7; Figure 10). The spectra also tend to be flatter in the NE limb than in the SW limb. On the other hand, the other parameters of the mathematical models, such as the break energy of bknpower and curvature β of logparabola, do not show

significant azimuthal variations. The steepening of the nonthermal spectra from the center of the limb to large azimuthal angles, however, could be explained by a higher cutoff energy instead of a smaller photon index of any physical models in the center of the limb (the photon index α is indeed larger in the center, Figure 11; also revealed in previous works, e.g., Rothenflug et al. 2004; Miceli et al. 2009, 2014, 2016). This is also consistent with the shape of the PDF, i.e., both higher cutoff energy E_{cutoff} and steeper slope Γ in the center of the limb where the particle acceleration seems the most efficient (Figure 12(d), (e)). E_{cutoff} and Γ are, in general, positively correlated with each other (Figure 13). Consistent with the discussion in Section 4.1, this correlation suggests that when the turbulent magnetic field is stronger (Reynoso et al. 2013) and the CR acceleration is the most efficient, the nonlinear effect tends to be the most significant, making the particles accelerate to higher energy. In the mean time, the PDF becomes steeper, which may be a result of many processes, as listed at the end of Section 4.1.

SN1006 is close enough that proper motion measurements over a timeline of ~ 10 years has led to an accurate measurement of the expansion velocity of a few bright filaments (e.g., Katsuda et al. 2009; Winkler et al. 2014). In this paper, based on the relatively low-resolution *NuSTAR* data, we are discussing the synchrotron emission in much larger regions than the width of the filaments with expansion velocity measured, so we do not have a quantitative comparison between the synchrotron emission parameters and the

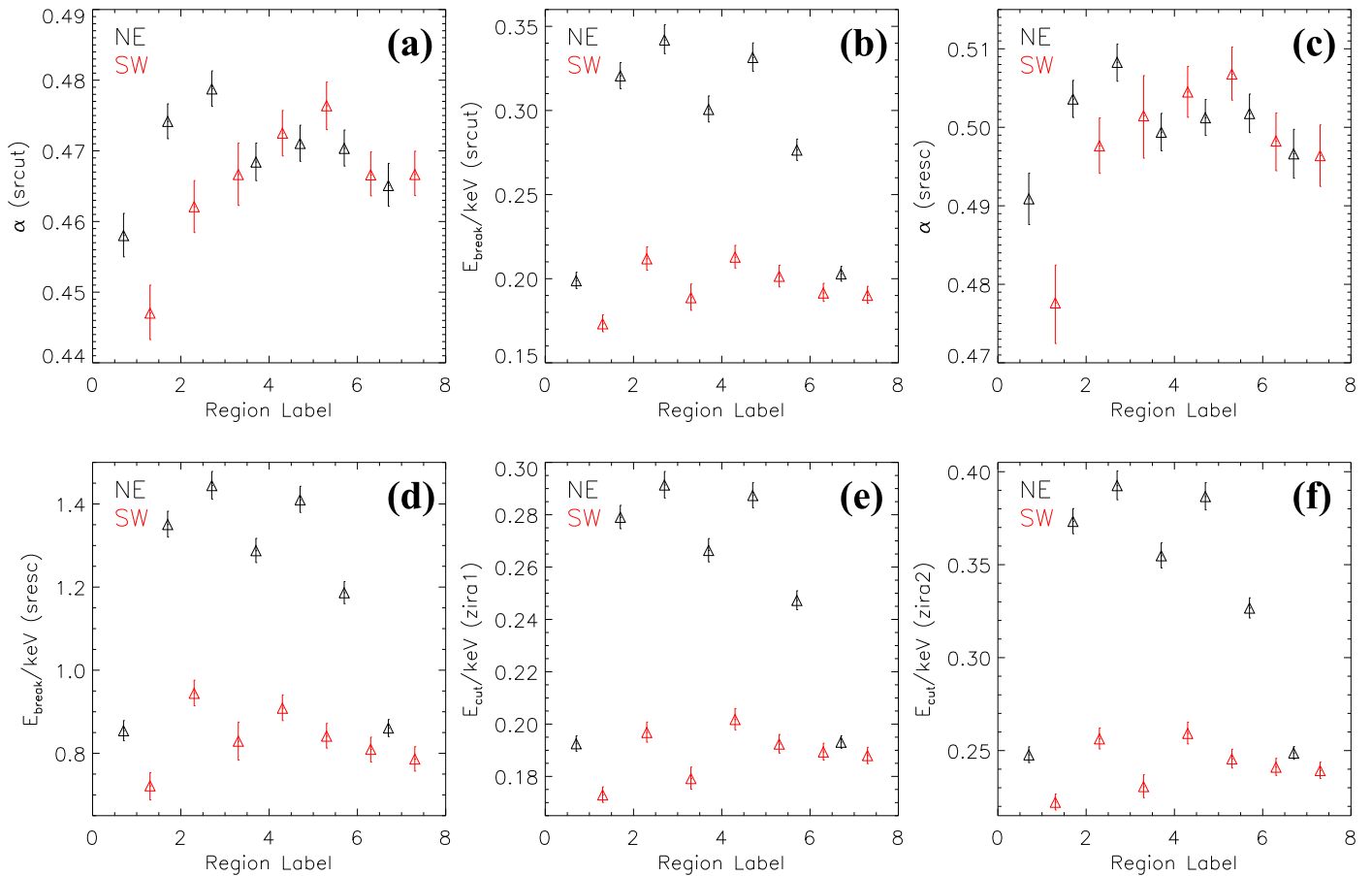


Figure 11. Azimuthal variation of the parameters of the srcut, sresc, zira1, and zira2 models fitted to only the X-ray spectra. The best-fit spectra are presented in panels (c)–(f) of Figure 5, while the model parameters are listed in Tables 5 and 6.

expansion velocity. Nevertheless, the overall trend of the azimuthal variations of the cutoff energy of the PDF and the expansion velocity seems quite different from what has been found in Tycho’s SNR, where they show a clear positive correlation, which indicates that the CR acceleration is age-limited instead of loss-limited in this much younger and also Type Ia SNR (Lopez et al. 2015). Oppositely, the cutoff energy of the PDF in SN1006, at least in the NE limb, seems to be anticorrelated with the expansion velocity (Winkler et al. 2014). Further investigations of the spatial variations and the relation between the cutoff energy and the shock velocity require high-resolution maps of the synchrotron emission parameters, which could resolve individual filaments. Right now, based on the *NuSTAR* data, we speculate that the efficient CR acceleration in the nonthermal limbs may have decelerated the shock significantly, producing the apparent anticorrelation between the cutoff energy and the expansion velocity. This idea is supported by the fact that the highest expansion velocity is observed along the southeast periphery of the SNR, where little nonthermal emission has been detected (Winkler et al. 2014).

We do not find any significant correlations between the radio (or hard X-ray) flux and the spectral fitting parameters (such as the cutoff frequency of srcut) as revealed by previous works (e.g., Katsuda et al. 2010; Li et al. 2015). This is probably because the low angular resolution of *NuSTAR* has smoothed the small-scale variation (as small as the size of the filaments) of synchrotron emission parameters.

The cutoff energy in both the emission spectrum and the PDF are significantly higher in the NE limb than in the SW limb (Figures 11(b), (d), (e), (f), 12(e)), apparently indicating that the particle acceleration is more efficient in the NE limb. Furthermore, we have also noticed that the slope of both the emission spectrum and the default PDF in SW regions 1–3 is systematically flatter than those in regions with similar angular distances from the center of the limb (Figures 11(a), (c), 12(d)). The χ^2/dof of any models of these three regions is also systematically higher than other regions (Figure 7), with nearly all of the models underpredicting the X-ray emission at $\gtrsim 8$ keV (Figure 5). The SNR shocks in these regions have been reported to interact with an HI cloud, producing slightly increased absorption column density and decreased cutoff frequency (Miceli et al. 2014). It is thus likely that the encounter of a high density cloud in the northern part of the SW limb has significantly slowed down the shock (consistent with proper motion measurements of the nonthermal filaments, e.g., Winkler et al. 2014) and made the particle acceleration less efficient. In the mean time, the interaction with the cloud has created some nonlinear effects, making the PDF flatter and the radiative cooling less efficient.

4.3. Compare with γ -Ray Observations

Type Ia SNRs are typically not strong γ -ray emitters because of the relatively low ambient density. SN1006 is one of the few Type Ia SNRs well resolved in both TeV by ground-based

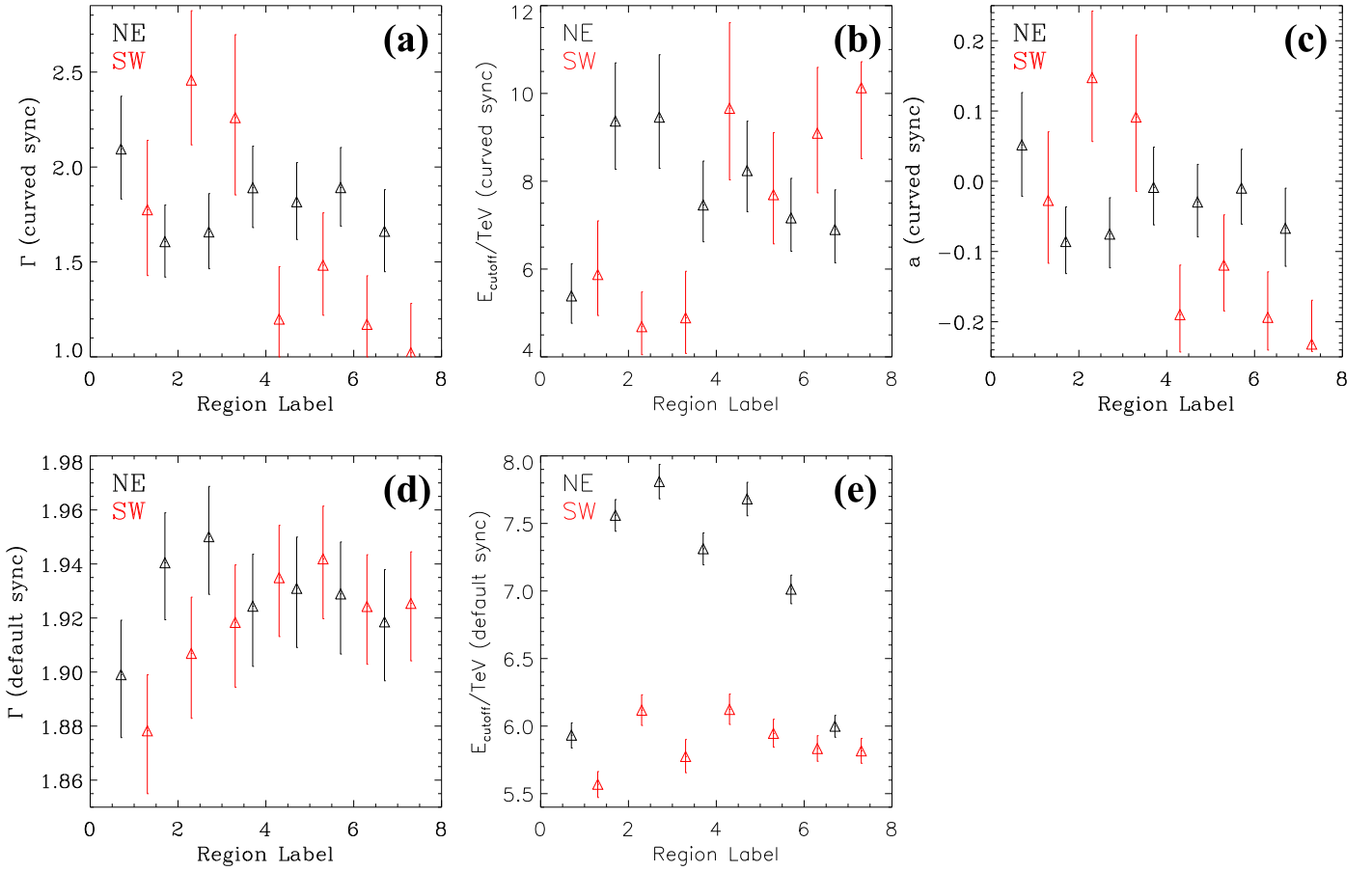


Figure 12. Azimuthal variation of the parameters of the synchrotron emission model with default (“default sync”) or curved (“curv sync”) particle energy distributions fitted to both the X-ray and radio spectra. The best-fit spectra are presented in Figure 8, while the model parameters are listed in Table 7.

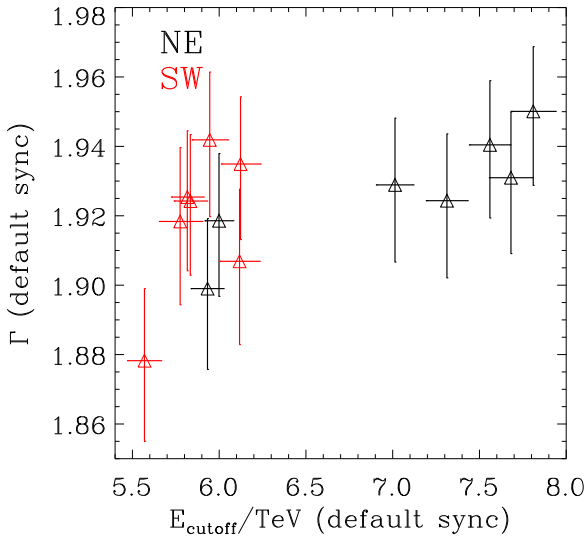


Figure 13. Index (Γ) and cutoff energy (E_{cutoff}) of the “default” PDF.

Cherenkov Telescopes (e.g., Acero et al. 2010) and in GeV by *Fermi-LAT* (e.g., Xing et al. 2016; Condon et al. 2017).

Our *NuSTAR* observations for the first time confirm that the energy distribution of the CR electrons responsible for the synchrotron X-ray emission beyond 10 keV does not show a significant concavity or curvature, and could be described with a single power law with an exponential cutoff. The emission spectrum, however, is significantly steeper than those in GeV

($\Gamma \approx 1.79$, Condon et al. 2017) and TeV ($\Gamma \approx 2.3$, Acero et al. 2010) bands (Figure 6). Therefore, although a pure leptonic scenario based on inverse Compton (IC) emission of the same electron population can well describe the GeV spectrum, it tends to underpredict the emission at TeV (Acero et al. 2010). On the other hand, a pure hadronic model requires a flatter proton spectrum than the electron spectrum in order to match the flatter TeV emission spectrum. The required magnetic field is also consistent with our assumptions of $B_{\text{tot}} \sim 100 \mu\text{G}$. However, such a model requires a very large fraction ($\sim 20\%$) of the SN energy goes into CRs, which is close to the upper limit, if not unexpected. A mixed model, with the leptonic component dominating the low-energy γ -ray range (typically $\lesssim (0.1-1)$ TeV), and the hadronic component (via the decay of π^0 meson) dominating the higher energy range, is probably more reasonable to describe the broadband nonthermal spectrum (Acero et al. 2010). Such a model requires an even higher cutoff energy of the CR protons than the pure hadronic model, which is ~ 100 TeV, or more than 10 times of the cutoff energy of CR electrons as revealed by our X-ray observations (Table 7). The maximum energy of CR electrons is thus likely largely limited by synchrotron radiative loss, which does not affect the CR hadrons.

Although the TeV morphology of SN1006 seems roughly symmetric (Acero et al. 2010), the GeV emission is much stronger in the NE limb than in the SW limb, with the latter not even firmly detected (Condon et al. 2017). Although the CR electron populations responsible for the GeV (via IC loss) and

hard X-ray emissions (via synchrotron loss) may not be exactly the same, the significant asymmetry in GeV flux is, in general, consistent with our X-ray measurements, which indicates much lower cutoff energy in the SW limb probably due to the interaction with the denser ISM in this direction (Figure 12(e)). The significant difference in the GeV flux and the consistency of the TeV spectra in the NE and SW limbs are difficult to be explained with a single leptonic or hadronic scenario.

5. Summary and Conclusions

We present deep *NuSTAR* observations of the NE and SW nonthermal limbs of the Galactic SNR SN1006. We discover three sources with X-ray emission detected at $\gtrsim 50$ keV. Two of them have significant multiwavelength counterparts and are identified as background AGNs, while one is not identified with online catalogs and is likely a Galactic source. We also extract the *NuSTAR* spectra from a few regions along the nonthermal limbs and jointly analyze them with the *XMM-Newton* spectra at $kT \gtrsim 0.8$ keV and the radio data corrected for the missing flux. Below we summarize our major results and conclusions on the nonthermal emission from the two limbs:

1. The X-ray spectral slope is clearly steeper in the *NuSTAR* band than in the *XMM-Newton* band. The broadband X-ray spectra cannot be characterized with a power law with just a single break. Instead, they can be characterized with a curved-power-law model (“logparabola”). When fitted with a synchrotron emission model, however, the shape of the broadband X-ray spectra is consistent with the synchrotron emission from a single population of CR electrons with a power-law energy distribution and an exponential cutoff. The power-law index of the PDF is typically 1.88–1.95 for both limbs, but the cutoff energy is significantly higher in the NE limb (~ 7.5 TeV v.s. ~ 6.0 TeV), assuming the same magnetic field of $\sim 100 \mu\text{G}$. The data presented in this paper, with the radio flux only measured at one frequency, do not support a significant variation of the slope of the PDF at different energies on a scale of $\sim 2'$, although a concavity of the PDF is previously claimed with the radio spectra and the higher-resolution *Chandra* data.
2. The loss-limited models do not provide a better fit to the nonthermal X-ray spectra than the escape-limited models, as suggested by Miceli et al. (2013) in the study of a few of the brightest nonthermal filaments. In some regions in the SW limb, the loss-limited models always underpredict the X-ray emissions at $\gtrsim 8$ keV. Because of the lower angular resolution of *NuSTAR*, we have to extract spectra from larger regions covering both the highly structured filaments and the diffuse nonthermal emission from the limbs. Therefore, we conclude that synchrotron radiative losses are only important in the X-ray band in limiting the particle acceleration at the brightest filaments, which apparently have the most compressed and amplified magnetic field so the highest cooling rate.
3. Some of the synchrotron emission parameters show significant spatial variations. The broadband X-ray spectrum is, in general, flatter in the center of the NE and SW limbs and becomes steeper at larger azimuthal angles. The flatter emission spectrum in the center of the limb, however, is caused by a significantly higher cutoff

energy of the CR electron PDF, instead of a flatter slope of the PDF. The cutoff energy also seems to be anticorrelated with the expansion velocity measured from the proper motion of some filaments. This trend is opposite to what has been found in the Tycho’s SNR. In addition to the gradual azimuthal variation, we also find that the slopes of both the emission spectrum and the PDF are significantly smaller in three regions in the SW limb where the shock encounters a higher density ambient medium. Nearly all of the models underpredict the X-ray emission at $\gtrsim 8$ keV in these three regions, indicating a more complicated PDF of the accelerated CRs. Furthermore, the NE limb shows significantly higher cutoff energies in the PDF than the SW limb, indicating more efficient particle acceleration, which is consistent with the much brighter GeV γ -ray emission on this side. On the other hand, the TeV emission, which is largely contributed by the hadronic emission, is much more symmetric on the two nonthermal limbs. The morphology of the broadband nonthermal emission indicates that the asymmetry in the ambient medium and magnetic fields may have largely modified the leptonic CR emissions.

The authors acknowledge Kristy Dyer and Stephen Reynolds for providing their radio images of SN1006, Daniel Wik for his very helpful suggestions on *NuSTAR* background analysis, John Houck, Shuinai Zhang, Glenn E. Allen, and Michael Nowak for their help and discussions on the nonthermal emission models and the usage of ISIS, as well as Federico Fraschetti for scientific discussions. J.T.L. acknowledges the financial support from NASA through the grants NNX15AV24G, NNX15AM93G, SOF05-0020, 80NSSC18K0536, and NAS8-03060. The research leading to these results has received funding from the European Union’s Horizon 2020 Programme under AHEAD project (grant agreement n. 654215). Y.C. acknowledges the support by the 973 Program under grants 2017YFA0402600 and 2015CB857100, and the NSFC under grants 11773014, 11633007, and 11851305.

ORCID iDs

Jiang-Tao Li  <https://orcid.org/0000-0001-6239-3821>
 Jean Ballet  <https://orcid.org/0000-0002-8784-2977>
 Marco Miceli  <https://orcid.org/0000-0003-0876-8391>
 Ping Zhou  <https://orcid.org/0000-0002-5683-822X>
 Jacco Vink  <https://orcid.org/0000-0002-4708-4219>
 Yang Chen  <https://orcid.org/0000-0002-4753-2798>
 Joel N. Bregman  <https://orcid.org/0000-0001-6276-9526>

References

- Acero, F., Aharonian, F., Akhperjanian, A. G., et al. 2010, *A&A*, 516, 62
 Aharonian, F., Akhperjanian, A. G., Aye, K.-M., et al. 2005, *A&A*, 437, 135
 Allen, G. E., Houck, J. C., & Sturmer, S. J. 2008, *ApJ*, 683, 773
 Allen, G. E., Petre, R., & Gotthelf, E. V. 2001, *ApJ*, 558, 739
 An, H., Madsen, K. K., Westergaard, N. J., et al. 2014, *SpIE*, 9144, 1
 Bamba, A., Fukazawa, Y., Hiraga, J. S., et al. 2008, *PASJ*, 60, 153
 Bamba, A., Yamazaki, R., Ueno, M., & Koyama, K. 2003, *ApJ*, 589, 827
 Becker, R. H., Szymkowiak, A. E., Boldt, E. A., Holt, S. S., & Serlemitsos, P. J. 1980, *ApJ*, 240, 33
 Berezhko, E. G., & Ellison, D. C. 1999, *ApJ*, 526, 385
 Berezhko, E. G., Ksenofontov, L. T., & Völk, H. J. 2012, *ApJ*, 759, 12
 Blandford, R., & Eichler, D. 1987, *PhR*, 154, 1
 Blasi, P. 2013, *A&ARv*, 21, 70
 Brenneman, L. W., & Reynolds, C. S. 2006, *ApJ*, 652, 1028
 Caprioli, D. 2011, *JCAP*, 5, 26
 Caprioli, D. 2012, *JCAP*, 7, 38

- Caprioli, D., Blasi, P., Amato, E., & Vietri, M. 2009, *MNRAS*, **395**, 895
- Condon, B., Lemoine-Goumard, M., Acero, F., & Katagiri, H. 2017, *ApJ*, **851**, 100
- Dubner, G. M., Giacani, E. B., Goss, W. M., Green, A. J., & Nyman, L.-A. 2002, *A&A*, **387**, 1047
- Dyer, K. K., Cornwell, T. J., & Maddalena, R. J. 2009, *AJ*, **137**, 2956
- Dyer, K. K., Reynolds, S. P., Borkowski, K. J., Allen, G. E., & Petre, R. 2001, *ApJ*, **551**, 439
- Fraschetti, F., Katsuda, S., Sato, T., Jokipii, J. R., & Giacalone, J. 2018, *PhRvL*, **120**, 1101
- Harrison, F. A., Craig, W. W., Christensen, F. E., et al. 2013, *ApJ*, **770**, 103
- Helder, E. A., Vink, J., Bykov, A. M., et al. 2012, *SSRv*, **173**, 369
- Houck, J. C., & Denicola, L. A. 2000, *ASPC*, **216**, 591
- Katsuda, S., Petre, R., Long, K. S., et al. 2009, *ApJL*, **692**, 105
- Katsuda, S., Petre, R., Mori, K., et al. 2010, *ApJ*, **723**, 383
- Koyama, K., Petre, R., Gotthelf, E. V., et al. 1995, *Natur*, **378**, 255
- Li, J.-T., Decourchelle, A., Miceli, M., Vink, J., & Bocchino, F. 2015, *MNRAS*, **453**, 3953
- Li, J.-T., Decourchelle, A., Miceli, M., Vink, J., & Bocchino, F. 2016, *MNRAS*, **462**, 158
- Long, K. S., Reynolds, S. P., Raymond, J. C., Winkler, P. F., Dyer, K. K., & Petre, R. 2003, *ApJ*, **586**, 1162
- Lopez, L. A., Grefenstette, B. W., Reynolds, S. P., et al. 2015, *ApJ*, **814**, 132
- Massaro, E., Perri, M., Giommi, P., & Nesci, R. 2004, *A&A*, **413**, 489
- Miceli, M., Acero, F., Dubner, G., et al. 2014, *ApJL*, **782**, 33
- Miceli, M., Bocchino, F., Decourchelle, A., et al. 2013, *A&A*, **556**, 80
- Miceli, M., Bocchino, F., Iakubovskiy, D., et al. 2009, *A&A*, **501**, 239
- Miceli, M., Orlando, S., Pereira, V., et al. 2016, *A&A*, **593**, 26
- Morlino, G., Amato, E., Blasi, P., & Caprioli, D. 2010, *MNRASL*, **405**, 21
- Parizot, E., Marcowith, A., Ballet, J., & Gallant, Y. A. 2006, *A&A*, **453**, 387
- Reynolds, S. P. 1998, *ApJ*, **493**, 375
- Reynolds, S. P. 2008, *ARA&A*, **46**, 89
- Reynoso, E. M., Hughes, J. P., & Moffett, D. A. 2013, *AJ*, **145**, 104
- Rothenflug, R., Ballet, J., Dubner, G., et al. 2004, *A&A*, **425**, 121
- Wenger, M., Ochsenein, F., Egret, D., et al. 2000, *A&AS*, **143**, 9
- Wik, D. R., Hornstrup, A., Molendi, S., et al. 2014, *ApJ*, **792**, 48
- Winkler, P. F., & Long, K. S. 1997, *ApJ*, **491**, 829
- Winkler, P. F., Williams, B. J., Reynolds, S. P., et al. 2014, *ApJ*, **781**, 65
- Xing, Y., Wang, Z., Zhang, X., & Chen, Y. 2016, *ApJ*, **823**, 44
- Zirakashvili, V. N., & Aharonian, F. 2007, *A&A*, **465**, 695